Electronic Supplementary Information

Zn-Flux–Enabled Synthesis of Orthorhombic Kagome $YbFe_6Ge_6$: Yb Reduction and Magnetic Behavior

Rahul Meduri,[1] Grant R. Wilkinson,[2] Muhammad Z. Idrees,[3] Kaya Wei,[4] Sebastian A. Stoian,[3] Henry La Pierre,[4] Gregory T. McCandless,[1] Julia Y. Chan[1]*

[1]Department of Chemistry and Biochemistry, Baylor University, Waco, TX, 76798, United States

[2]School of Chemistry and Biochemistry, Georgia Institute of Technology, Atlanta, GA, 30332, United States

[3]Department of Chemistry, University of Idaho, Moscow, ID, 83844, United States

[4]National High Magnetic Field Laboratory, Tallahassee, FL, 32310, United States

*Corresponding author: Julia_Chan@baylor.edu

Synthesis of *o*-$YbFe_6Ge_6$

The elements Yb:Fe:Ge were weighed out in a 1.2:6:6 ratio with an excess 30 mol of Zn. The elements were then set into a Canfield alumina crucible,[1] and subsequently sealed in a fused silica tube under ~1/3 atm of Ar gas. The sealed silica tubes were then heated in a programmable furnace to 1100 °C at a rate of 150 °C/h and allowed to dwell for 24 h. The samples cooled to 900 °C at a rate of 5 °C/h and were then removed from the furnace, inverted and centrifuged to remove excess molten flux. Excess flux was etched in a 1:1 solution of HCl/H_2O.

Structural Determination

The crystal structure of *o*-$YbFe_6Ge_6$ was determined using single-crystal X-ray diffraction (SCXRD). Data were collected on a Bruker D8 Quest Kappa diffractometer equipped with an IμS microfocus Mo Kα source (λ = 0.71073 Å) and a PHOTON III CPAD area detector. Raw data frames were integrated using the Bruker SAINT program, and a multi-scan absorption correction was applied with SADABS.[2] The initial structural model was obtained via intrinsic phasing in SHELXT,[3] followed by full-matrix least-squares refinement in SHELXL.[4] Crystallographic data and refinement parameters for each structure are summarized in Table S1, and atomic coordinates and displacement parameters are provided in Table S2.

Powder X-ray diffraction data (Figure S1) were collected with a Bruker D2 Phaser (Cu Kα radiation, λ = 1.54184 Å) operating at 30 kV/10 mA equipped with a LYNXEYE XE-T detector. An exposure time of 1 s and a step size of 0.02° were used to collect over a 2θ range of 5-80°. TOPAS was used for the Rietveld refinement.[5]

Energy-dispersive X-ray spectroscopy (EDS) was performed on single crystals of *o*-$YbFe_6Ge_6$ to assess the extent of Zn incorporation into the structure. Measurements were collected using a VERSA 3D focused ion beam–scanning electron microscope with an acceleration voltage of 30 kV and a spot size of 5. Ten distinct points on each crystal were analyzed. The averaged composition obtained was $Yb_{0.881(2)}Fe_{5.513(3)}Zn_{0.487(1)}Ge_{4.820(3)}$. The elemental ratios were normalized to (Fe + Zn) = 6, because the transition metal sites do not partake in the structural disorder characteristic of this structure type. The possibility of sub-stoichiometric amounts of Yb and Ge were explored for deviations from the 1-6-6 formula. However the refined model does not support this. Only a small amount of positional disorder is observed with a refined occupational ratio of ~90% Yb1/Ge5: ~10% Yb2/Ge6.

We evaluated the possibility of Zn substituting on the Ge sites, given that Fe and Zn exhibit sufficiently different X-ray scattering factors to be distinguishable. As shown in the simulated powder diffraction, the compositionally constrained models revealed pronounced differences in the intensities of the (040) and

(021) reflections (Figure S2). Notably, Zn substitution on the Fe sites produces a clear increase in the intensities of these peaks. On this basis, and consistent with the elemental ratios obtained from EDS analysis, we modeled Zn occupancy on the Fe sites.

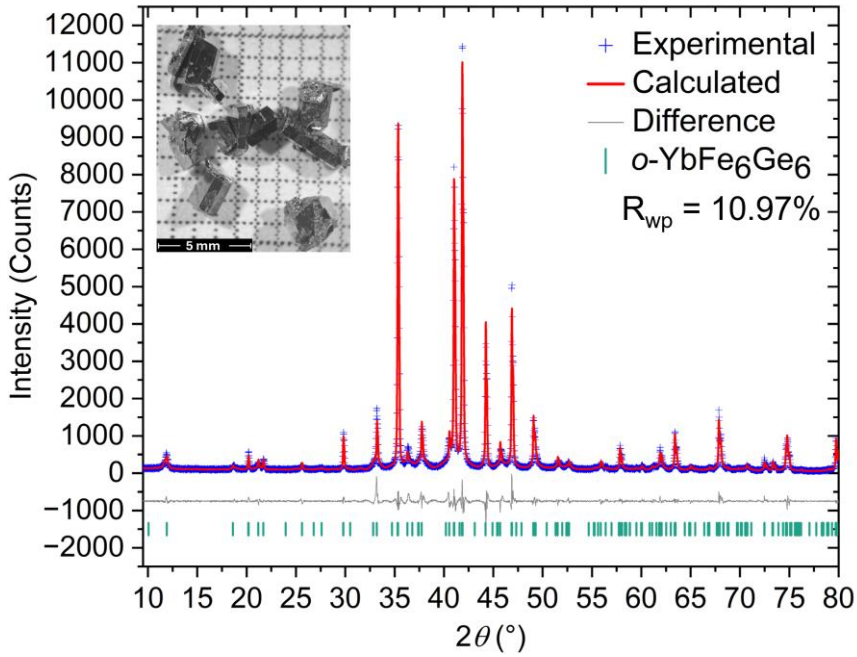

Figure S1. Refined powder diffraction pattern of orthorhombic $YbFe_6Ge_6$. (inset) Crystals of Zn-grown *o*-$YbFe_6Ge_6$.

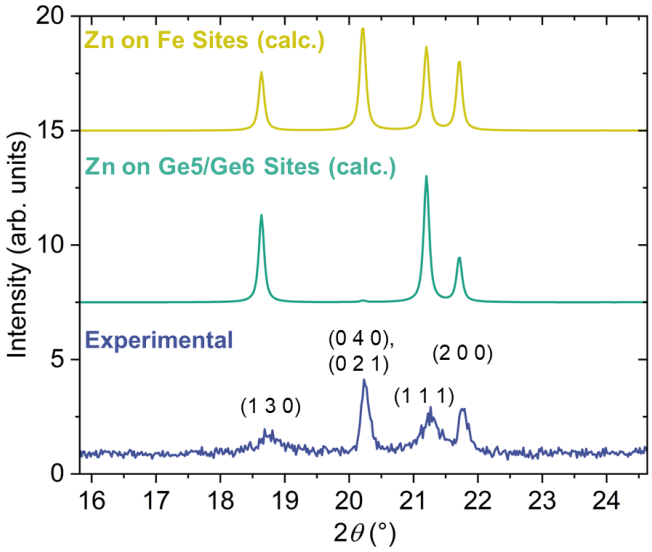

Figure S2. Comparison of experimental powder diffraction data with two calculated *o*-$YbFe_6Ge_6$ powder patterns with relevant *hkl* reflections labeled. The two calculated patterns are labeled according to whether the Zn was constrained on the Ge sites or if it was constrained on the Fe sites.

X-ray Absorption Spectroscopy

Measurement and Data Processing

The oxidation state reference $YbCl_3$ was purchased from a commercial supplier and used without further purification. X-ray absorption spectroscopy (XAS) measurements were performed at the Stanford Synchrotron Radiation Lightsource (SSRL) under dedicated operating conditions (3.0 GeV, 5%, 500 mA with continuous top-off injections) on BL 7-3. Incident energy was selected using a liquid nitrogen cooled double crystal Si(220) monochromator at the ϕ = 90º orientation. The monochromator was detuned to between 50-70% of the maximum incident flux 1 keV above the nominal edge energy to reject higher harmonic reflections.

Samples for analysis were prepared in an argon glovebox at SSRL and were diluted with boron nitride (BN) to ~1:5 analyte to BN ratio by mass. BN was dried at >250 ºC under vacuum for 24 h prior to use and shipped to SSRL in vacuum sealed ampoules. The analyte-BN mixture was ground to homogeneity in an agate mortar and pestle and uniformly loaded into a 1/64" thick aluminum plate (Al-6061) with a 0.156 x 0.75 in^2 oval window that was first half-sealed with 0.5 mil Kapton tape. The sample holder was then fully sealed with Kapton tape and screwed into an aluminum bracket before being removed from the glovebox and immediately submerged in liquid nitrogen. The bracket assembly was then transported to the beamline, attached to the sample rod, and loaded into a closed-cycle He cryostat (Oxford) under flow of He gas, at a 45º angle to the direction of the incident beam. The sample chamber was then cycled three times to remove residual atmosphere before allowing to cool to a floor temperature of ~7 K. Samples were then aligned in the beam and measurements performed in transmission mode with a beam size of 1 x 10 mm^2. The hutch and detector setup were as previously described,[6] and incident energy was calibrated using the first inflection point of the Cu *K*-edge (8979 eV)[7] of a Cu metal foil placed downstream of the sample and measured simultaneous to the sample data.

To ensure no beam damage occurred during measurement, three scans at ±30 eV of the nominal Yb L_3-edge (8944 eV)[7] for the $YbCl_3$ oxidation state reference and *o*-$YbFe_6Ge_6$ analyte prior to full analysis and no evidence of photo-oxidation or -reduction was noted for either compound. Full measurements were taken of each sample over a range of ±100 eV of the nominal Yb L_3-edge to provide sufficient data for normalization of the pre- and post-edge regions. Full scans were performed in triplicate and independently calibrated and normalized prior to averaging using Athena.[8] The averaged datasets are presented below. Edge energies are reported as the inflection point in the rising edge unless otherwise specified.

Fitting Details

The Yb L_3-edge spectrum of *o*-$YbFe_6Ge_6$ was curve-fit using an implementation of the lmfit Python library in a home-built code.[9] The step was modelled with an error-function of fixed σ (2.5 eV) and amplitude (1 a.u.) with the center allowed to freely refine. The peaks were modelled with pseudo-Voigt functions with a fixed Gaussian:Lorentzian ratio of 1:1. The full-width at half-maximum (FWHM) of the peaks was constrained to twice the core-hole lifetime of the Yb L_3-edge absorption of (σ = 4.20 eV)[8] and the centers and amplitudes were allowed to freely refine. The results of the fit are provided in Table S1 and the fit spectrum is shown in Figure S5.

Table S1. Fit parameters for Yb L_3-edge of *o*-$YbFe_6Ge_6$ using a two-peak model.

Peak	*Center (eV)*	*σ (eV)*[a]	*Amplitude (a.u.)*	*Peak Height (a.u.)*[b]	*Peak Area*[c,d]
Step	8946.76(4)	2.5	1[a]	—	—
Peak 1	8938.27(5)	4.20	4.40(4)	0.413(4)	4.57(4)
Peak 2	8944.846(16)	4.20	16.36(7)	1.535(6)	16.99(7)

[a]Fixed during fitting procedure

[b]Corresponds to maximum of peak

[c]Calculated as $(2\sigma)\times(\text{Peak Height})\times 0.25([\pi/\ln(2)]^{1/2}+\pi)$ where the final term ≈1.318

[d]Error propagated from relative error of peak height

The calculation of the Yb^{3+} percentage in the system, denoted n_f, can be calculated with the following equation[10]:

$$n_f = \frac{A(Yb^{3+})}{A(Yb^{3+}) + A(Yb^{2+})} \quad \text{(S1)}$$

Where $A(Yb^{3+})$ and $A(Yb^{2+})$ are the areas of the peaks associated with Yb^{3+} (Peak 2) and Yb^{2+} (Peak 1) respectively. The value calculated based on the fit of the spectrum is n_f = 0.79(8). A modification of this equation[11] can also be used to calculate the *effective* oxidation state of Yb in the compound:

$$z = 2 + \frac{A(Yb^{3+})}{A(Yb^{3+}) + A(Yb^{2+})} \quad \text{(S2)}$$

Where z is the *effective* oxidation state.

Magnetic Properties

Temperature-dependent magnetic susceptibility χ(T) and isothermal magnetization M($\mu_0 H$) measurements were performed for single crystals using a Quantum Design vibrating sample magnetometer (VSM) magnetic property measurement system (MPMS). M(μ_0H) measurements were performed at constant temperatures under applied magnetic fields μ_0H from −7 to 7 T. χ(T) measurements were done under constant magnetic fields for a range of temperatures from 1.8 to 300 K.

^{57}Fe Mössbauer Spectroscopy

The field- and temperature-dependent Mössbauer, or Nuclear Gamma Resonance, spectra were recorded using two spectrometers operated in a constant acceleration mode. One of these instruments was equipped with a liquid helium cooled Janis 8DT SuperVariTemp cryostat fitted with an 8 T superconducting coil manufactured by American Magnetics. The magnetic field was applied parallel to the propagation direction of the 14.4 keV gamma rays used to detect the Mössbauer effect. Spectra recorded at 4.2 K were obtained by submerging the samples in liquid helium. Higher temperatures were maintained using a Cryocon 22C temperature controller fitted with a Cernox sensor while the sample was kept in a flow of helium gas. The isomer shift values are reported against the center of a spectrum recorded at room temperature for an alpha iron foil. The same spectrum was also used to calibrate the velocity scale. The sample consisted of ~5 mg ground *o*-$YbFe_6Ge_6$ powder dispersed in ~100 mg eicosane contained in a custom plastic cup. The eicosane functioned as inert support.

The spectra were analyzed using the WMOSS program (See Co, formerly Web Research Co, Edina, MN) as well using IgorPro codes developed in-house. While the simulations of the zero-field spectra considered a single spectral component, the field dependent spectra were rationalized using the Voigt-based method to account for the distribution of hyperfine fields (HFD) developed by Rancourt *et al*.[12,13] In this model, the HFD spectra may be thought as originating from a sum of a large number of elemental component for which the resonances have a Γ linewidth and the individual hyperfine field values follow a Gaussian distribution centered at z_0 and has full width at half-maximum (FWHM) dz. In addition, the intensities of the observed resonances is determined by the h_{13} and h_{23} parameters which account for the outer/inner and middle/inner line intensities of six-line, magnetic spectrum.

Up to 4 T, the spectra recorded in an applied magnetic field are readily rationalized considering two components with equal spectral area. While for one component the hyperfine splitting increases with the applied field, for the other, it decreases with the applied field, see Figure 3 and S7. Superficially, this behavior is consistent with the expected antiferromagnetic ordering of iron sites. However, our analysis reveals a more complicated behavior than that anticipated for a simple colinear alignment of iron sublattices' moments with the applied field. Thus, increasing the applied field leads to a dramatic increase in the distribution of hyperfine fields which suggests that the magnetic order begins to break down. In addition, the high-field, 6 - 8 T, spectra are not well reproduced when only two components are considered. Instead, these spectra were simulated by considering an additional component which at 6 T accounted for ~ 16 %, and at 8 T for ~ 33 % of the spectral area, respectively. While the applied field has little influence on the magnitude of the hyperfine field of this component, the enhanced amplitude of the middle ($\Delta m = 0$) resonances suggest that the hyperfine field of this component is essentially perpendicular to the applied field. These observations suggest that perhaps above 6 T, we witness the onset of a metamagnetic transition even though no obvious changes are observed in the magnetization data.

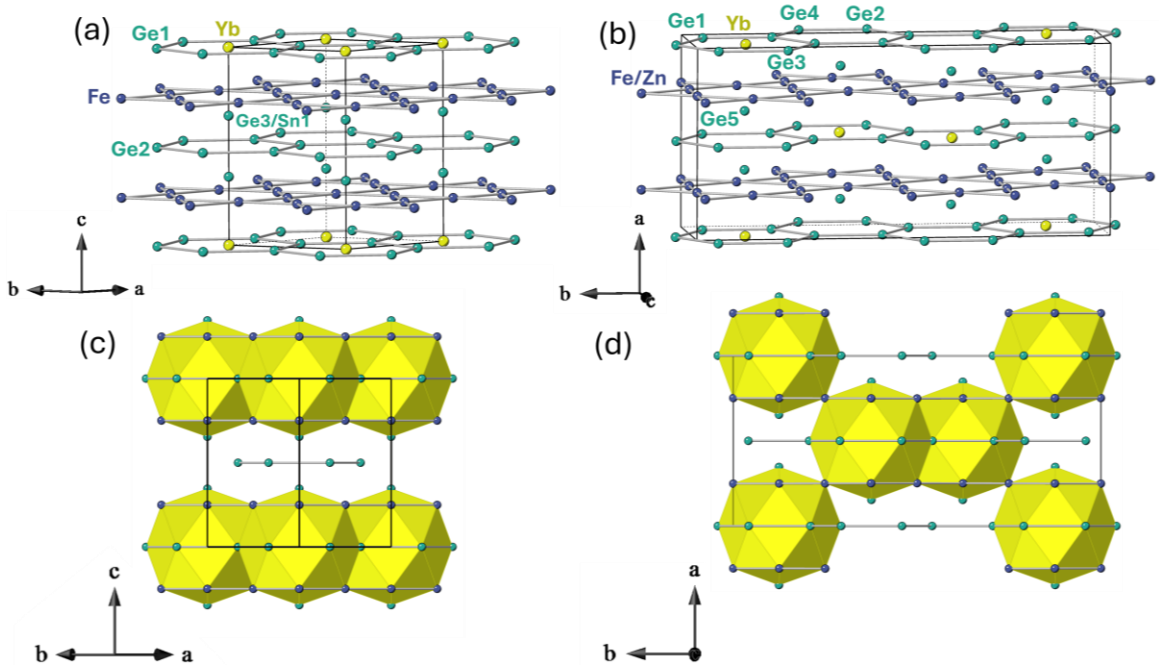

Figure S3. Unit cells of (a) *h*-$YbFe_6Ge_6$ and (b) *o*-$YbFe_6Ge_6$, disordered sites omitted for clarity. Ordering scheme of the Yb atoms in (c) *h*-$YbFe_6Ge_6$ and (d) *o*-$YbFe_6Ge_6$ along the *ab*-plane and *b*-direction respectively.

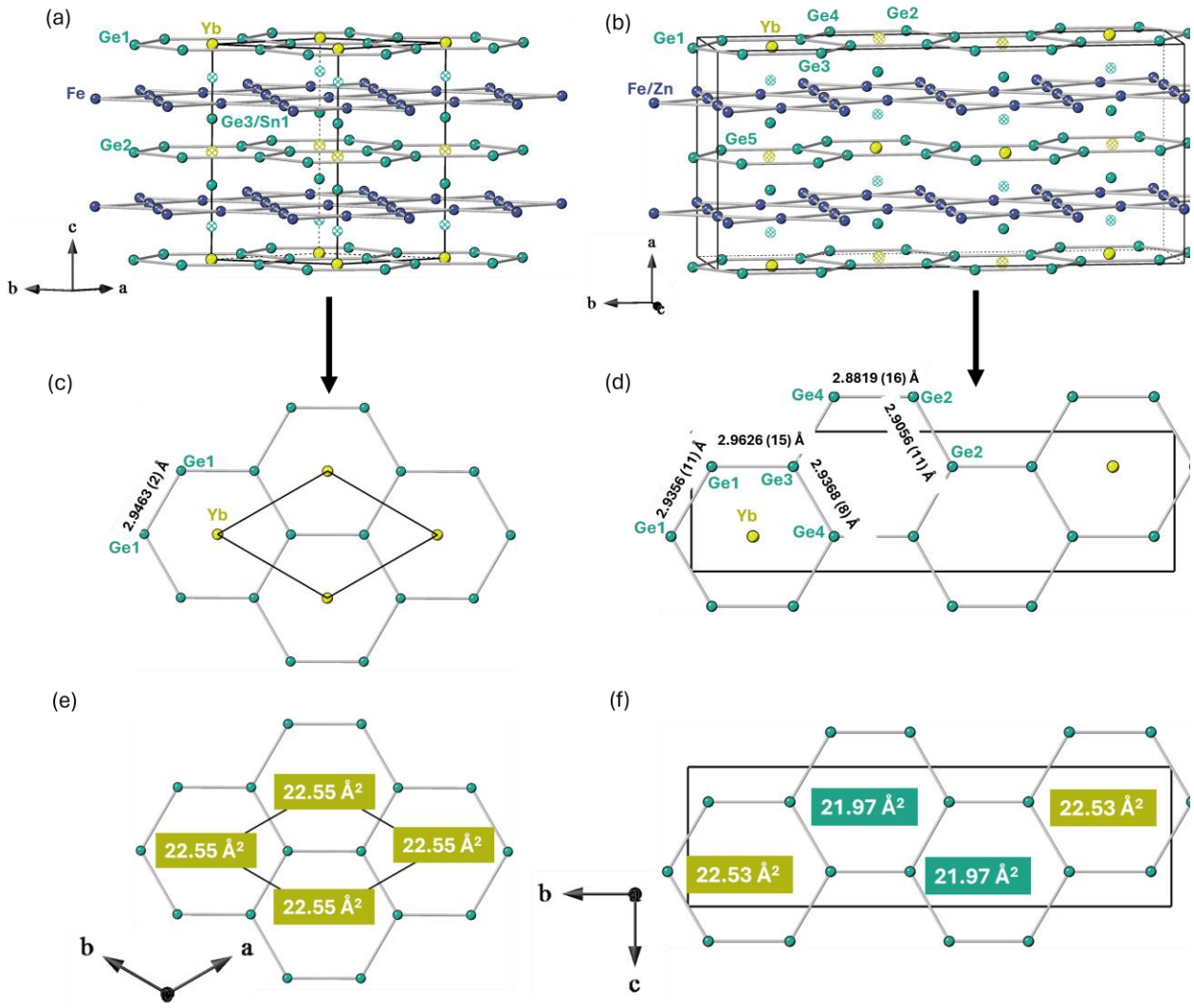

Figure S4. Unit cells of (a) *h*-$YbFe_6Ge_6$ and (b) *o*-$YbFe_6Ge_6$. Selected interatomic distances to highlight differences in honeycomb sublattice in (c) *h*-$YbFe_6Ge_6$ and (d) *o*-$YbFe_6Ge_6$. Areas of both Yb occupied and unoccupied hexagons of the honeycomb lattice for (e) *h*-$YbFe_6Ge_6$ and (e) *o*-$YbFe_6Ge_6$. A yellow shaded text box indicates an Yb atom resides in the hexagon and green shaded text box indicates an unoccupied hexagon. The solid black line shows the corresponding unit cells.

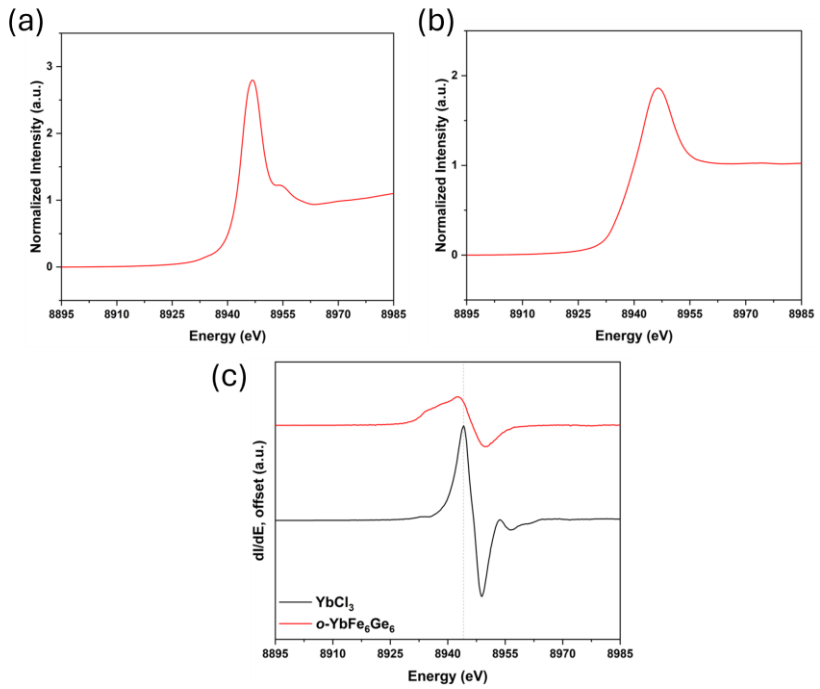

Figure S5. (a) Normalized Yb L_3-edge spectrum of $YbCl_3$.(b) Normalized Yb L_3-edge spectrum of *o*-$YbFe_6Ge_6$. (c) First derivatives of Yb L_3-edge spectra of $YbCl_3$ (black) and *o*-$YbFe_6Ge_6$ (red). Grey dashed line indicates the edge energy of $YbCl_3$.

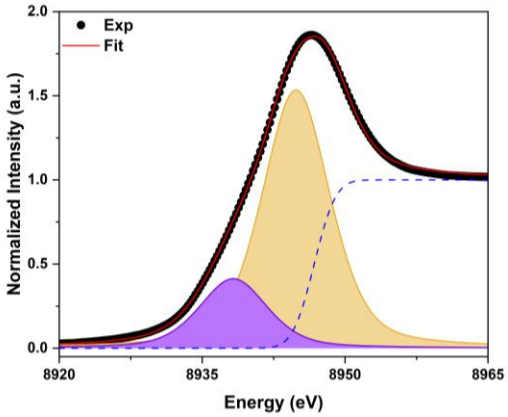

Figure S6. Fit of the Yb L_3-edge spectrum of *o*-$YbFe_6Ge_6$ using a two-peak model. Peak 1 is shown in magenta, Peak 2 in beige, and the step function is shown as a dotted blue line.

Table S2. Crystallographic Data and Refinement Parameters for $YbFe_{5.52}Zn_{0.48}Ge_6$.

Empirical Formula	$YbFe_{5.52}Zn_{0.48}Ge_6$
Crystal System	Orthorhombic
Space group	*Cmcm*
a (Å)	8.1799(12)
b (Å)	17.541(2)
c (Å)	5.0739(6)
Volume (Å^3)	728.03(16)
Z	4
Density (g/cm^3)	8.651
Abs. Coefficient (mm^{-1})	49.15
Crystal size (mm^3)	0.01 x 0.04 x 0.05
Theta range (°)	2.3 – 30.5
Index Range	
h	-11 → 11
k	-24 → 24
l	-7 → 7
Number of Reflections	15627
Unique Reflections	653
Data/Restraints/Parameters	653/1/50
R_{int}	0.076
$\Delta\rho_{max}/\Delta\rho_{min}$ (e Å^{-3})	2.51/-2.70
GoF	1.19
$R_1[F^2 > 2\sigma(F^2)]$	0.026
$wR(F^2)$	0.071

Table S3. Atomic Coordinates and Atomic Displacement Parameters of $YbFe_{5.52}Zn_{0.48}Ge_6$

	Wyckoff Site	x	y	z	U_{iso}*/U_{eq}	Occ.
Yb1	4*c*	0	0.12740(3)	¼	0.00766(17)	0.8945(13)
Yb2	4*c*	½	0.1213(2)	¼	0.00766(17)	0.1055(13)
Fe1	8*d*	¼	¼	0	0.0078(3)	0.92
Zn1	8*d*	¼	¼	0	0.0078(3)	0.08
Fe2	8*e*	0.24711(12)	0	0	0.0078(3)	0.92
Zn2	8*e*	0.24711(12)	0	0	0.0078(3)	0.08
Fe3	8*g*	0.24821(12)	0.12505(6)	¾	0.0078(3)	0.92
Zn3	8*g*	0.24821(12)	0.12505(6)	¾	0.0078(3)	0.08
Ge1	4*c*	0	0.04210(6)	¾	0.0069(3)	1
Ge2	4*c*	½	0.04038(6)	¾	0.0107(3)	1
Ge3	4*c*	0	0.21099(6)	¾	0.0081(3)	1
Ge4	4*c*	½	0.20467(7)	¾	0.0096(3)	1
Ge5	8*g*	0.34659(11)	0.12380(5)	¼	0.0078(2)	0.8945(13)
Ge6	8*g*	0.8474(9)	0.1243(4)	¼	0.0078(2)	0.1055(13)

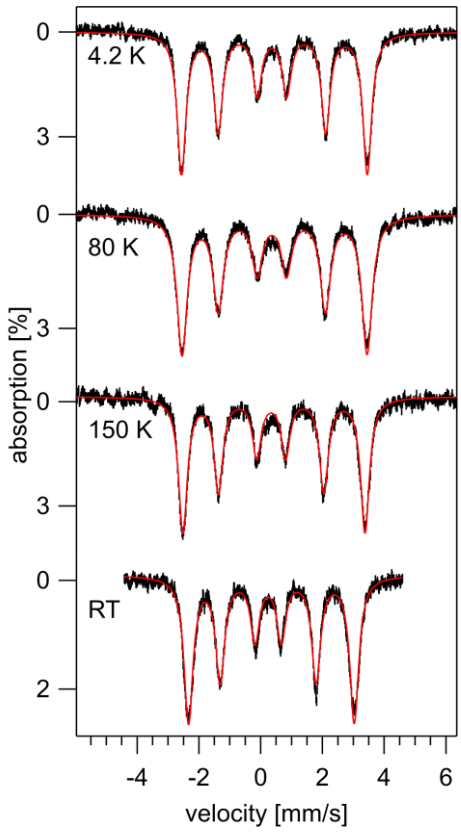

Figure S7. Temperature dependent Mössbauer spectra recorded in zero-field for *o*-$YbFe_6Ge_6$.

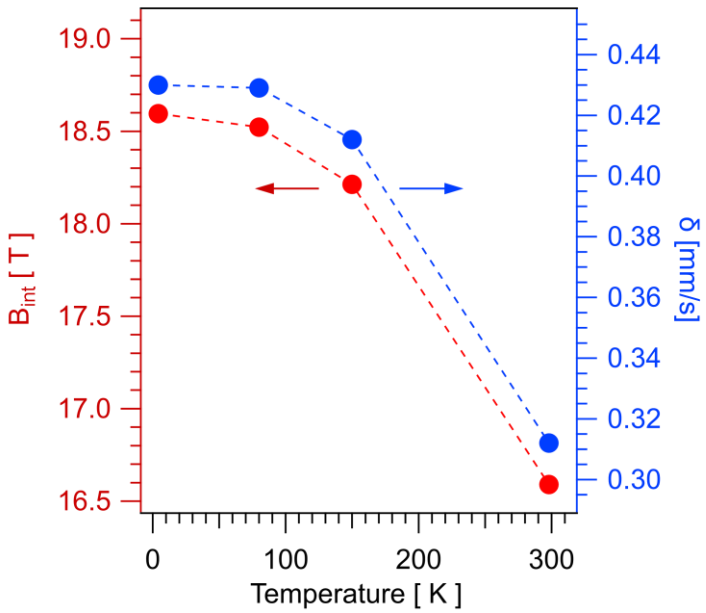

Figure S8. Temperature dependence of the hyperfine fields, B_{int}, and of the isomer shift derived from the simulations of the spectra recorded in zero field.

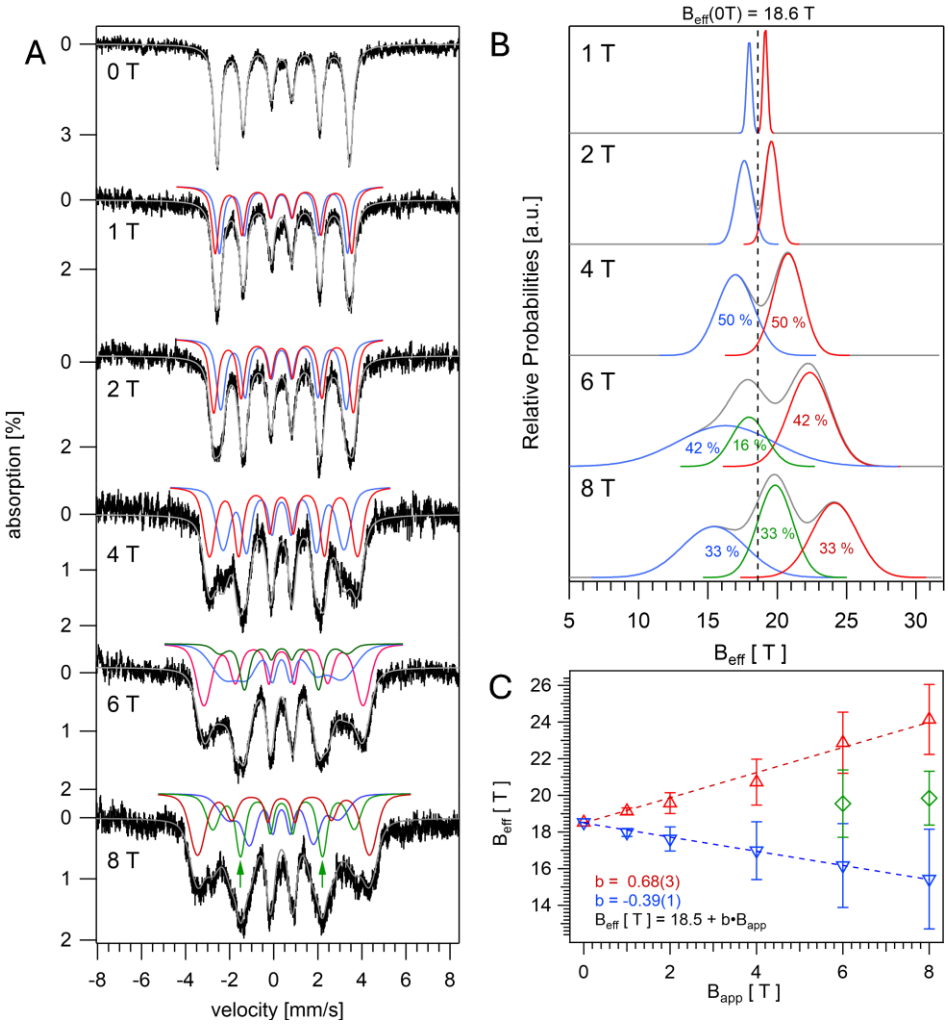

Figure S9. (A) Field dependent Mössbauer spectra recorded at 4.2 K for *o*-$YbFe_6Ge_6$. The solid grey lines are theoretical spectra obtained from the sum of the individual components shown in red, blue, and green above the corresponding experimental spectrum. These simulations were obtained using the parameters listed in Table S3. The vertical arrows of the 8 T spectrum highlight the enhancement of the middle ($\Delta m = 0$) resonances for the green spectral component. (B) Distribution of hyperfine fields derived from the simulations of the field-dependent data The solid vertical dashed line indicates the hyperfine field, B_{int} = 18.6 T, observed in zero-field. (C) Field-dependence of the effective hyperfine fields as function of the applied field. The error bars indicate the full width at half-maximum (dz) of the HFD inferred for the corresponding spectral component.

Table S4. Hyperfine structure parameters derived from the analysis of the Mössbauer spectra.

Temp. [K]	**Field** [T]	**site**	**Γ** [mm/s]	**δ** [mm/s]	**ε_0** [mm/s]	**z_0** [T]	**dz** [T]	**$h_{2/3}$**	**$h_{1/3}$**	**%**
4.2	0	red	0.34	0.43	0.08	18.6	-	1.6	2.3	100
80	0	red	0.38	0.43	0.09	18.5	-	1.6	2.4	100
150	0	red	0.34	0.41	0.09	18.2	-	1.6	2.3	100
298	0	red	0.35	0.31	0.10	16.6	-	1.6	2.3	100
4.2	1	red	0.35	0.43	0.08	19.1	0.4	1.6	2.3	50
		blue	0.35	0.43	0.08	18.0	0.4	1.6	2.3	50
4.2	2	red	0.35	0.43	0.08	19.6	1.1	1.6	2.2	50
		blue	0.35	0.43	0.08	17.6	1.4	1.6	2.2	50
4.2	4	red	0.35	0.43	0.08	20.8	2.5	1.8	2.3	50
		blue	0.35	0.43	0.08	17.0	3.1	1.8	2.3	50
4.2	6	red	0.35	0.43	0.08	22.9	3.5	1.3	2.7	42
		blue	0.35	0.43	0.08	16.2	8.2	1.3	2.7	42
		green	0.35	0.43	0.08	19.6	2.9	4.0	1.0	16
4.2	8	red	0.35	0.43	0.08	24.1	3.8	2.0	1.5	33
		blue	0.35	0.43	0.08	15.4	5.5	2.0	1.5	33
		green	0.35	0.43	0.08	19.5	2.9	1.2	4.0	33

References

1. Canfield, P. C.; Kong, T.; Kaluarachchi, U. S.; Jo, N. H., Use of Frit-Disc Crucibles for Routine and Exploratory Solution Growth of Single Crystalline Samples. *Philos. Mag.,* **2016,** *96*, 84-92.
2. Krause, L.; Herbst-Irmer, R.; Sheldrick, G. M.; Stalke, D., Comparison of Silver and Molybdenum Microfocus X-ray Sources for Single-Crystal Structure Determination. *J. Appl. Crystallogr.,* **2015,** *48*, 3-10.
3. Sheldrick, G., SHELXT - Integrated Space-group and Crystal-Structure Determination. *Acta Crystallogr. A.,* **2015,** *71*, 3-8.
4. Sheldrick, G., Crystal Structure Refinement with SHELXL. *Acta Crystallogr. C.,* **2015,** *71*, 3-8.
5. Coelho, A., TOPAS and TOPAS-Academic: An Optimization Program Integrating Computer Algebra and Crystallographic Objects Written in C++. *J. Appl. Crystallogr.,* **2018,** *51*, 210-218.
6. Boggiano, A. C.; Chowdhury, S. R.; Roy, M. D.; Bernbeck, M. G.; Greer, S. M.; Vlaisavljevich, B.; La Pierre, H. S., A Four-Coordinate Pr^{4+} Imidophosphorane Complex. *Angew. Chem. Int. Ed.,* **2024,** *63*, e202409789.
7. Thompson, A.; Attwood, D.; Gullikson, E.; Howells, M.; Kim, K.-J.; Kirz, J.; Kortwright, J.; Lindau, I.; Liu, Y.; Pianetta, P.; Robinson, A.; Scofield, J.; Underwood, J.; Williams, G.; Winick, H., *X-Ray Data Booklet*. 3 ed.; Center for X-Ray Optics and Advanced Light Source, Lawrence Berkeley National Laboratory: Berkeley, CA, 2009.
8. Ravel, B.; Newville, M., *ATHENA*, *ARTEMIS*, *HEPHAESTUS*: data analysis for X-ray absorption spectroscopy using *IFEFFIT*. *J. Synchrotron Radiat.,* **2005,** *12*, 537-541.
9. Newville, M.; Otten, R.; Nelson, A.; Stensitzki, T.; Ingargiola, A.; Allan, D.; Fox, A.; Carter, F.; Michal; Osborn, R.; Pustakhod, D.; Weigand, S.; Ineuhaus; Aristov, A.; Glenn; Mark; mgunyho; Deil, C.; Hansen, A. L. R.; Pasquevich, G.; Foks, L.; Zobrist, N.; Frost, O.; Stuermer; Jaskula, J.-C.; Caldwell, S.; Eendebak, P.; Pompili, M.; Nielsen, J. H.; Persaud, A., lmfit/lmfit-py: 1.3.1. **2024**.
10. He, A.; Wille, E. L. K.; Moreau, L. M.; Thomas, S. M.; Lawrence, J. M.; Bauer, E. D.; Booth, C. H.; Kauzlarich, S. M., Intermediate Yb Valence in the Zintl Phases $Yb_{14}MSb_{11}$ (M = Zn, Mn, Mg): XANES, Magnetism, and Heat Capacity. *Phys. Rev. Mater.,* **2020,** *4*, 114407.
11. Utsumi, Y.; Sato, H.; Ohara, S.; Yamashita, T.; Mimura, K.; Motonami, S.; Shimada, K.; Ueda, S.; Kobayashi, K.; Yamaoka, H.; Tsujii, N.; Hiraoka, N.; Namatame, H.; Taniguchi, M., Electronic Structure of Kondo Lattice Compounds $YbNi_3X_9$ (X= Al, Ga) Studied by Hard X-ray Spectroscopy. *Phys. Rev. B,* **2012,** *86*, 115114.
12. Lagarec, K.; Rancourt, D. G., A New Model for Multidimensional Distributions of Hyperfine Parameters in Mössbauer Spectroscopy. **1999,** 215-220.
13. Ping, J. Y.; Rancourt, D. G., Absolute Quantitative Analysis by Mössbauer Spectroscopy. *Hyperfine Interact.,* **1992,** *71*, 1437-1440.